Oxidation Behavior of Refractory AlNbTiVZr$_{0.25}$ High-Entropy Alloy

Nikita Yurchenko, Evgeniya Panina, Sergey Zherebtsov[ID], Gennady Salishchev[ID] and Nikita Stepanov *[ID]

Laboratory of Bulk Nanostructured Materials, Belgorod State National Research University, Belgorod 308015, Russia; yurchenko_nikita@bsu.edu.ru (N.Y.); 985376@bsu.edu.ru (E.P.); zherebtsov@bsu.edu.ru (S.Z.); salishchev@bsu.edu.ru (G.S.)

* Correspondence: stepanov@bsu.edu.ru; Tel.: +7-4722-58-54-16

Abstract: Oxidation behavior of a refractory AlNbTiVZr$_{0.25}$ high-entropy alloy at 600–900 °C was investigated. At 600–700 °C, two-stage oxidation kinetics was found: Nearly parabolic oxidation (n = 0.46–0.48) at the first stage, transitioned to breakaway oxidation (n = 0.75–0.72) at the second stage. At 800 °C, the oxidation kinetics was nearly linear (n = 0.92) throughout the entire duration of testing. At 900 °C, the specimen disintegrated after 50 h of testing. The specific mass gains were estimated to be 7.2, 38.1, and 107.5, and 225.5 mg/cm^2 at 600, 700, and 800 °C for 100 h, and 900 °C for 50 h, respectively. Phase compositions and morphology of the oxide scales were analyzed using X-ray diffraction (XRD) and scanning electron microscopy (SEM). It was shown that the surface layer at 600 °C consisted of the V$_2$O$_5$, VO$_2$, TiO$_2$, Nb$_2$O$_5$, and TiNb$_2$O$_7$ oxides. Meanwhile, the scale at 900 °C comprised of complex TiNb$_2$O$_7$, AlNbO$_4$, and Nb$_2$Zr$_6$O$_{17}$ oxides. The oxidation mechanisms operating at different temperatures were discussed and a comparison of oxidation characteristics with the other alloys was conducted.

Keywords: high entropy alloys; refractory; oxidation; complex oxides

1. Introduction

The so-called high-entropy alloys based on the refractory elements (refractory high-entropy alloys, RHEAs) are considered as candidates for high-temperature applications [1–5]. Some of them have high strength at T $\geq$ 1000 °C and thus can potentially operate at higher temperatures than commercial nickel-based superalloys [2,5–13]. Some RHEAs are sufficiently ductile at room temperature even in tension [14–18] and can be cold rolled [19–22]. However, refractory elements and their alloys are generally vulnerable to oxidation. A number of studies focused on oxidation behavior of different RHEAs [23–33] have demonstrated that some of them possess much better oxidation resistance than conventional refractory alloys; however, the oxidation behavior strongly depended on the alloy composition and testing conditions. Note that the vast majority of the performed research was conducted at temperatures of T $\geq$ 1000 °C [23–28,33].

Much less attention has been paid to the oxidation resistance of RHEAs at lower temperatures. For instance, an oxidation behavior of a series of Al$_x$TiZrNbHfTa (x = 0–1) RHEAs was examined at temperatures of 700, 900, 1100, and 1300 °C [22]. It was found that at 700 and 900 °C the TiZrNbHfTa alloy exhibited rapid oxidation—the so-called pesting phenomenon. The oxide layer detached easily from the bulk material and the formation of voids on the specimen surface was observed. An addition of Al increased the oxidation resistance and suppressed pesting. Similar behavior was found in the Hf$_{0.5}$Nb$_{0.5}$Ta$_{0.5}$Ti$_{1.5}$Zr alloy at 600–1000 °C [20]. Bulk samples of the alloy disintegrated into powder

already after 5 h of oxidation. Therefore, additional studies of the oxidation behavior of RHEAs at T < 1000 °C are required.

These studies are especially needed for RHEAs, which have a potential for operation at temperatures below 1000 °C. For instance, one of the perspective alloys of this group of RHEAs can be the AlNbTiVZr$_x$ alloys and, particularly, the AlNbTiVZr$_{0.25}$ alloy, where the B2 matrix phase contains a small amount of the Zr$_5$Al$_3$ phase particles [34]. The AlNbTiVZr$_{0.25}$ alloy showed a promising combination of properties for potential structural applications, namely low density (5.57 g/cm^3), high specific strength at room temperature, and 800 °C (244 and 154 kPa m^3/kg, respectively), and reasonable compression ductility (~10%) at room temperature [34]. The high strength of the alloy at ambient and elevated temperatures was attributed to a strong solid solution strengthening induced by Zr and the B2 ordered matrix phase [34]. In addition, the structure and mechanical properties of the AlNbTiVZr$_x$ alloys were found to be quite stable during long-term exposures at 800 °C or 1000 °C [35]. The reason for the sufficiently high phase stability was the presence of Zr, which prevented any phase transformations due to the formation of its own stable phases, like Zr$_5$Al$_3$ and ZrAlV-type C14 Laves.

In this study, we investigated the oxidation behavior of the AlNbTiVZr$_{0.25}$ high-entropy alloy at potential operating temperatures of 600–900 °C in order to obtain an extended estimation of its performance as a high-temperature material.

2. Materials and Methods

The alloy with a nominal composition of AlNbTiVZr$_{0.25}$ was produced by arc melting of the elements in a low-pressure, high-purity argon atmosphere inside a water-cooled copper cavity. The purities of the alloying elements were no less than 99.9 at.%. The produced ingot of the alloy measured ~6 × 12 × 40 mm^3. The as-cast ingot was homogenized at 1200 °C for 24 h; hereafter this condition was referred to as the initial one. Prior to the homogenizing, the ingot was encapsulated in a vacuumed (10^{-2} torr) quartz tube filled with titanium chips to prevent any oxidation.

Specimens for oxidation tests with nominal dimensions of 7 × 7 × 2.5 mm^3 were cut using an electric discharge machine from the ingot with the initial microstructure. Specimen surfaces were subsequently mechanically polished using a MasterMet (Buehler, Lake Bluff, IL, USA) colloidal silica suspension and finally ultrasonically cleaned in isopropanol. Oxidation tests were carried out in a Nabertherm furnace (LT 5/12/P320, Nabertherm, Lilienthal/Bremen, Germany) under static lab air at 600, 700, and 800 °C for 100 h, and 900 °C for 50 h. During the testing process, specimens were placed in alumina crucibles, oxidized at the mentioned temperatures, and removed from the furnace after 0.5, 1, 5, 10, 20, 50, and 100 h of the oxidation test for mass measurements. The mass of specimens before and after oxidation was measured using an HR-200 analytic balance (A&D Company, Ltd., Tokyo, Japan) with an accuracy of 0.1 mg to characterize the oxidation kinetics.

Phase identification of the oxides in the scales was performed by XRD using a RIGAKU Ultima IV diffractometer (Rigaku Corporation, Tokyo, Japan) with Cu-Kα radiation. Additionally, surfaces and cross-sectional morphologies of the specimens were examined by SEM. SEM investigations were carried out using either an FEI Quanta 600 FEG (Thermo Fisher Scientific, Brno, Czech Republic) or a Nova NanoSEM 450 microscope (Thermo Fisher Scientific, Brno, Czech Republic); both instruments were equipped with a back-scattered electron (BSE) and an energy-dispersive X-ray spectroscopy (EDS) detector. The volume fraction of the different phases was measured by a Digimizer Image Analysis Software (MedCalc Software, Ostend, Belgium) using SEM-BSE images.

3. Results

3.1. Initial Microstructure

Detailed information on the structure of the AlNbTiVZr$_{0.25}$ alloy has been reported elsewhere [34], thus only a brief description is presented here. Figure 1a shows the XRD pattern of the AlNbTiVZr$_{0.25}$

alloy in the initial (annealed at 1200 °C for 24 h) condition. In the XRD pattern, the Bragg peaks belonging to two phases, namely B2 and Zr_5Al_3, were found; the lattice parameters of B2 and Zr_5Al_3 phases were a = 0.3203 nm and a = 0.7996 nm, c = 0.5374 nm, respectively. Figure 1b shows the SEM-BSE image of the $AlNbTiVZr_{0.25}$ alloy. The alloy consisted of two structural constituents: (i) B2 grains (labeled with 1 in Figure 1b) with the average size of ~80 μm and the chemical composition close to that of the alloy (Table 1) and (ii) light-grey (Zr, Al)-rich particles (labeled with 2 in Figure 1b; Table 1) identified as the Zr_5Al_3 phase located both along the boundaries of the B2 grains as a discontinuous network and as separate particles or clusters of these particles in the B2 grains interior. The estimated volume fraction of the Zr_5Al_3 phase was ~5% (Table 1).

(a)   (b)
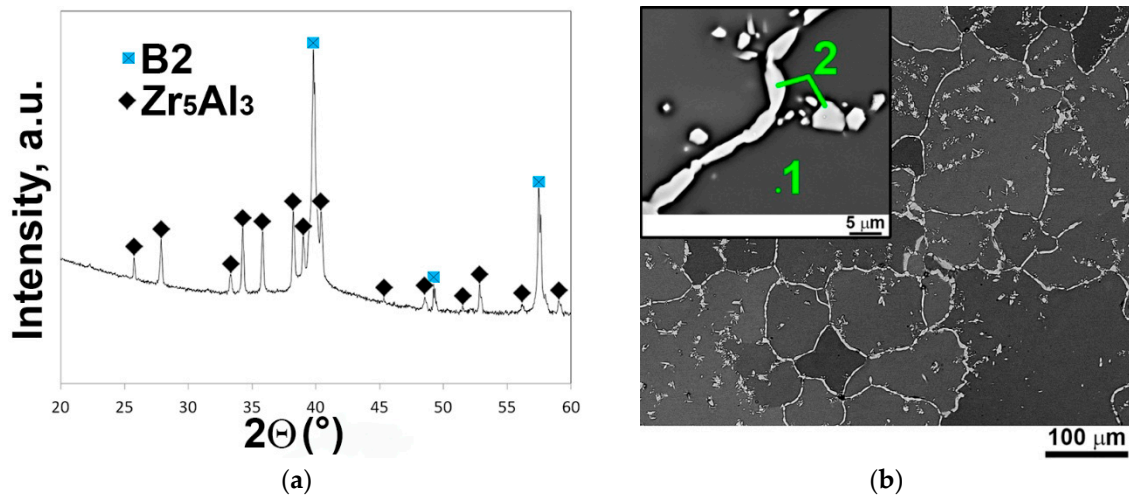
Figure 1. (**a**) X-ray diffraction (XRD) pattern and (**b**) SEM-back-scattered electron (BSE) image of the $AlNbTiVZr_{0.25}$ alloy in the initial state. Chemical compositions of the denoted regions were given in Table 1.

Table 1. Chemical compositions of the corresponding phases of the $AlNbTiVZr_{0.25}$ alloy in the initial state.

| Elements (at.%)		Al	Nb	Ti	V	Zr	Volume Fraction (%)
No.	Constituents Designation						
1	Grains	24.0	23.1	25.2	23.1	4.6	95 ± 2
2	Light-gray particles (Zr_5Al_3 phase)	38.2	14.0	11.4	4.4	32.0	5 ± 1
	Alloy composition	25.0	22.4	24.0	21.9	6.7	-

3.2. Oxidation Behavior

Figure 2a shows the isothermal oxidation kinetics of the $AlNbTiVZr_{0.25}$ alloy at 600, 700, 800, and 900 °C in terms of specific mass gain vs time. Images of the samples after testing at 600, 700, and 800 °C for 100 h, and 900 °C for 50 h are also shown (Figure 2c). Testing at 900 °C was interrupted after 50 h due to the significant disintegration of the sample. After oxidation, the specific mass gains were 7.2, 38.1, and 107.5, and 225.5 mg/cm^2 at 600, 700, and 800 °C for 100 h, and 900 °C for 50 h, respectively. The mass curves in Figure 2a were fitted to a general oxidation law [36]:

$$\Delta m = kt^n$$

where Δm is the specific mass gain, k is the oxide growth rate constant, t is time, and n is the time exponent. The best fit for 600 °C and 700 °C was found to be mixed parabolic-linear behavior (n = 0.67 for 600 °C, and n = 0.73 for 700 °C) with k = 0.31 mg/cm^2 $h^{0.67}$ and k = 1.30 mg/cm^2 $h^{0.73}$, respectively. The best fit for 800 °C was close to linear (n = 0.92) behavior with k = 1.57 mg/cm^2 $h^{0.92}$. The rate of

mass gain per unit surface area during oxidation at 900 °C followed a near-parabolic dependence with n = 0.52 and k = 29.68 mg/cm^2 h$^{0.52}$.

The oxidation behavior was also plotted in a double logarithmic scale in Figure 2b. At 600 °C, the alloy demonstrated nearly parabolic kinetics (n = 0.46) in the range of 0–20 h but then the oxidation rate increased significantly (n = 0.75). Similar behavior was found at 700 °C: Nearly parabolic kinetics (n = 0.48) observed from 0 to 5 h changed by mixed parabolic-linear (n = 0.72) one at longer time of testing. At 800 °C, a fairly rapid (n = 0.78) oxidation rate was observed throughout the entire duration of testing. At 900 °C, nearly parabolic kinetics (n = 0.56) was found. The obtained results could suggest the activation of multiple mechanisms during oxidation testing.
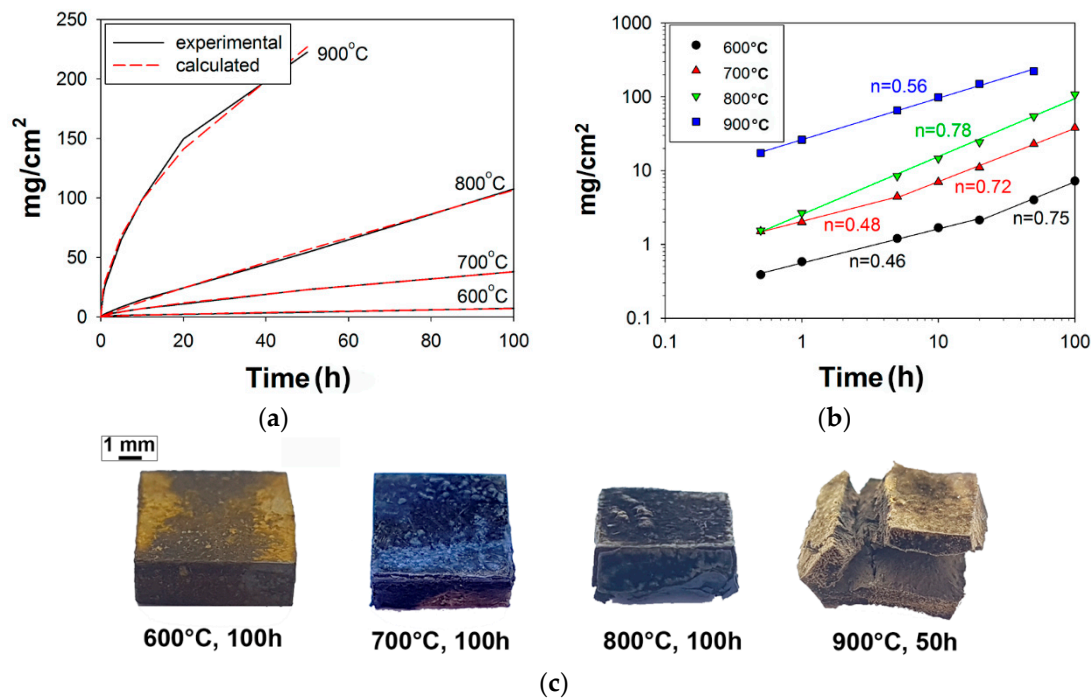
Figure 2. Specific mass gain plots of the AlNbTiVZr$_{0.25}$ alloy at 600, 700, and 800 °C for 100 h, and 900 °C for 50 h in static lab air using (**a**) linear and (**b**) double logarithmic scales; (**c**) images of the samples after testing at 600, 700, and 800 °C for 100 h, and 900 °C for 50 h.

3.3. Phase Analysis and Morphology of the Surface Layer

Figure 3 presents XRD patterns of the surface layers of the AlNbTiVZr$_{0.25}$ alloy oxidized at 600, 700, and 800 °C for 100 h, and 900 °C for 50 h. In Table 2 the identified oxides and their lattice parameters depending on the temperature are listed. The surface layer of the sample tested at 600 °C was composed of the V$_2$O$_5$ (space group #59) [37], VO$_2$ (space group #130) [38], TiO$_2$ (space group #136) [39], Nb$_2$O$_5$ (space group #15) [40], and TiNb$_2$O$_7$ (space group #12) [41] oxides; the peaks from the V$_2$O$_5$ and VO$_2$ oxides had the highest intensities. At 700 °C, in addition to the oxides observed at 600 °C, the ZrO$_2$ (space group #14) [42], AlNbO$_4$ (space group #12) [43], and Nb$_2$Zr$_6$O$_{17}$ (space group #46) [44] oxides emerged; intensities of the V$_2$O$_5$ and TiO$_2$ peaks were significantly lower in comparison with those at 600 °C. At 800 °C, the TiO$_2$, V$_2$O$_5$, and Nb$_2$O$_5$ oxides were not detected and the surface layer consisted of the VO$_2$ and ZrO$_2$ (low-intensity maximums) and TiNb$_2$O$_7$, AlNbO$_4$, and Nb$_2$Zr$_6$O$_{17}$ (high-intensity maximums) oxides. At 900 °C, the VO$_2$ and ZrO$_2$ oxides were not detected, and the surface layer was comprised mainly of the complex TiNb$_2$O$_7$, AlNbO$_4$, and Nb$_2$Zr$_6$O$_{17}$ oxides. Note that the positions of the diffraction peaks from the oxides were very close to that expected from the literature data on their crystal lattice parameters (Table 2).
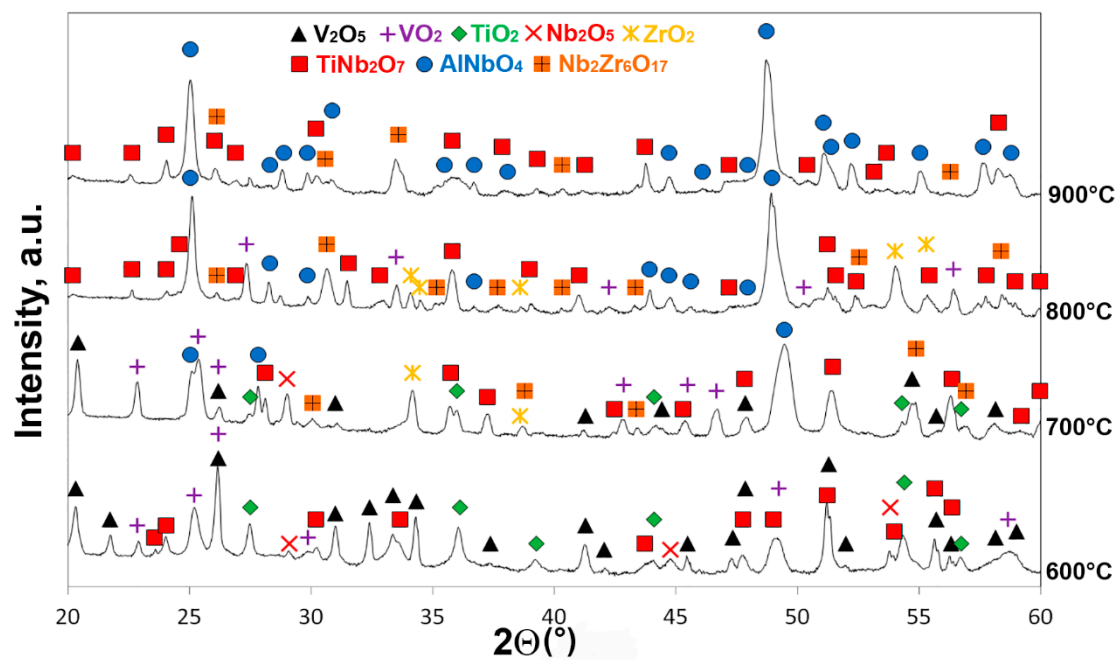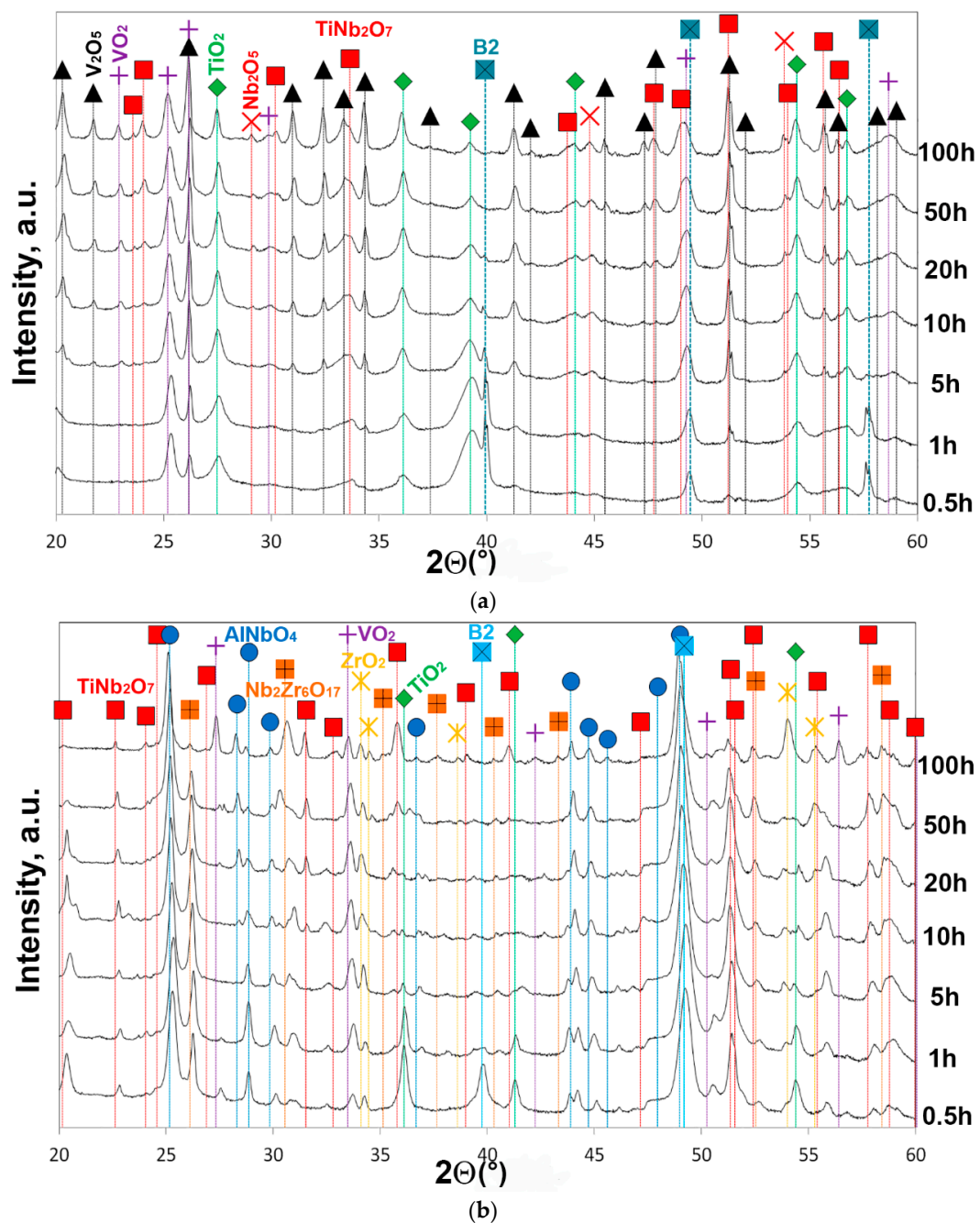
Figure 3. XRD patterns of the surface layers of the AlNbTiVZr$_{0.25}$ alloy oxidized at 600, 700, and 800 °C for 100 h, and 900 °C for 50 h.

Table 2. Data on the phase compositions of the surface layers and lattice parameters of the corresponding phases of the AlNbTiVZr$_{0.25}$ alloy oxidized at 600–900 °C.

Oxides	TiO$_2$	V$_2$O$_5$	Nb$_2$O$_5$	VO$_2$	ZrO$_2$	TiNb$_2$O$_7$	AlNbO$_4$	Nb$_2$Zr$_6$O$_{17}$
Lattice parameter (nm)	a = 0.4593, c = 0.2959 [39]	a = 0.3565, b = 1.1500, c = 0.4372 [37]	a = 1.2740, b = 0.4883, c = 0.5561 [40]	a = 0.8440, c = 0.7666 [38]	a = 0.5152, b = 0.5208, c = 0.5320 [42]	a = 2.0351, b = 0.3801, c = 1.1882 [41]	a = 1.2157, b = 0.3736, c = 0.6490 [43]	a = 4.0910, b = 0.4930, c = 0.5270 [44]
Temperature (°C)								
600	+ [1]	+	+	+	− [2]	+	−	−
700	+	+	+	+	+	+	+	+
800	−	−	−	+	+	+	+	+
900 (50 h)	−	−	−	−	−	+	+	+

[1] oxide is present; [2] oxide is absent.

Figure 4 shows the XRD patterns of the surface layers of the samples tested for 0.5–100 h at 600 °C (Figure 4a) and 800 °C (Figure 4b). According to Figure 4a, the initial (0.5 h) stage of oxidation at 600 °C was associated with the formation of the TiO$_2$ and VO$_2$ oxides; strong diffraction peaks belonging to the B2 phase were also observed. Starting from 5 h exposure, tiny peaks of the V$_2$O$_5$, TiNb$_2$O$_7$, and Nb$_2$O$_5$ oxides were found. The intensity of the oxides peaks, especially V-rich, rose gradually as time progressed. After 20 h, the Braggs peaks of the B2 phase vanished. At 800 °C, the surface layer at the initial (0.5 h) stage of oxidation consisted of the VO$_2$, TiO$_2$, ZrO$_2$, TiNb$_2$O$_7$, AlNbO$_4$, Nb$_2$Zr$_6$O$_{17}$ oxides and the B2 phase (Figure 4b). Increasing in time over 5 h resulted in the elimination of both the TiO$_2$ oxide and the B2 phase from the diffraction patterns. Note that the annealing time had not affected the position of diffraction peaks.

Figure 4. XRD patterns of the surface layers of the AlNbTiVZr$_{0.25}$ alloy oxidized at (**a**) 600 °C and (**b**) 800 °C for 0.5–100 h.

Figure 5 displays SEM-BSE images of the surfaces of the AlNbTiVZr$_{0.25}$ alloy oxidized at 600 and 800 °C for 0.5 and 100 h. Table 3 shows the chemical compositions of the surfaces. The beginning (0.5 h) of the oxidation process occurred differently at 600 and 800 °C. At 600 °C (Figure 5a), the oxidation developed heterogeneously, which is evident from the discrepancy in the topographic appearance of different grains. In addition, very fine oxide nodules were found (magnified insert in Figure 5a). At 800 °C (Figure 5b), the oxidation affected all the grains homogeneously. The oxide whiskers with the average transversal size of ~500 nm were found at the surface (insert in Figure 5b). At 600 °C (0.5 h) the surface layer contained, besides oxygen, almost equal amounts of Al, Nb, Ti, and V, and was depleted of Zr (Table 3). Meanwhile, at 800 °C, the surface layer was predominantly composed of V and O (Table 3).

After 100 h of oxidation at 600 °C, fine whisker-like oxides with the average transversal size of ~500 nm were found at the surface (Figure 5c). Similar oxide morphology was observed after oxidation at 800 °C (Figure 5d). However, the average transversal size of whiskers was ~1.5 μm. The chemical composition of the surfaces differed from that observed after 0.5 h of oxidation (Table 3). The surface of the sample after 100 h at 600 °C was enriched with V and O, while, nearly equal concentrations of Al, Nb, V, and Ti, and a high O content were found after oxidation at 800 °C (Table 3).

(**a**)   (**b**)

(**c**)   (**d**)
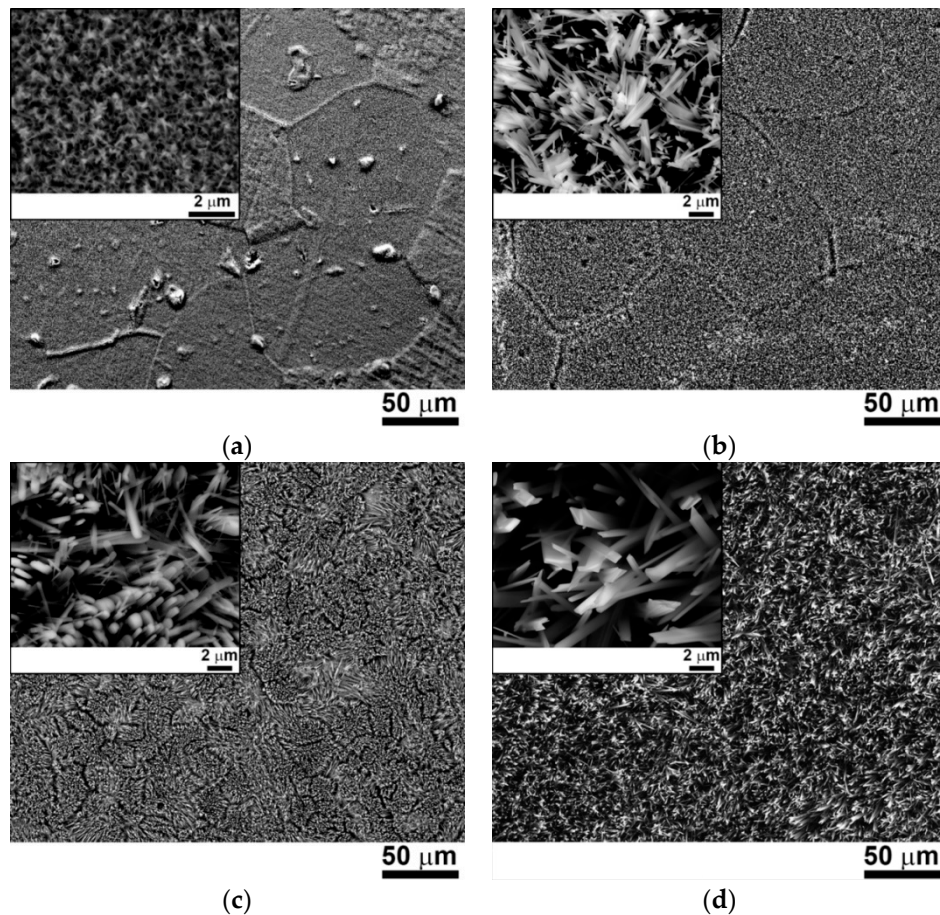
Figure 5. SEM-BSE images of the surface layers of the AlNbTiVZr$_{0.25}$ alloy oxidized for: 0.5 h at (**a**) 600 and (**b**) 800 °C; 100 h at (**c**) 600 and (**d**) 800 °C.

Table 3. Chemical compositions of the surface layers of the AlNbTiVZr$_{0.25}$ alloy oxidized at 600 and 800 °C for 0.5 and 100 h.

Elements (at.%)	Al	Nb	Ti	V	Zr	O
			0.5 h			
600 °C	14.1	12.7	12.8	14.7	1.1	44.6
800 °C	15.9	11.0	9.7	23.1	1.2	39.1
			100 h			
600 °C	3.6	4.4	4.6	27.9	0.6	58.9
800 °C	13.7	12.8	17.1	12.2	1.0	43.2

3.4. Cross-Sectional Morphologies

Figure 6 demonstrates SEM-BSE images and EDS maps of a cross-section of the AlNbTiVZr$_{0.25}$ alloy after oxidation at 600 °C for 100 h. The thickness of the oxide scale varied from ~15 μm to ~30 μm (Figure 6a). Multiple cracks in the oxide scale were found; the cracks seemed to nucleate on the scale-metal interface and propagated towards the surface (Figure 6a). According to the EDS

maps (Figure 6b–g), the external part of the oxide scale consisted of a thin (V, Zr)-rich oxide layer (OL) (Figure 6e,f), whereas its inner part was presented by a thick (Ti, Nb, Al)-rich OL (Figure 6b–d). Under the oxide scale, a wide (~100–150 μm) single-phase zone of the substrate with a homogeneous distribution of the constitutive elements was found. Underneath, the material contained particles enriched with Al and Zr (Figure 6b,f), and lean in Ti and V (Figure 6d,e), identified as the initial Zr_5Al_3 particles. Many fine pores were found in the material below the scale.
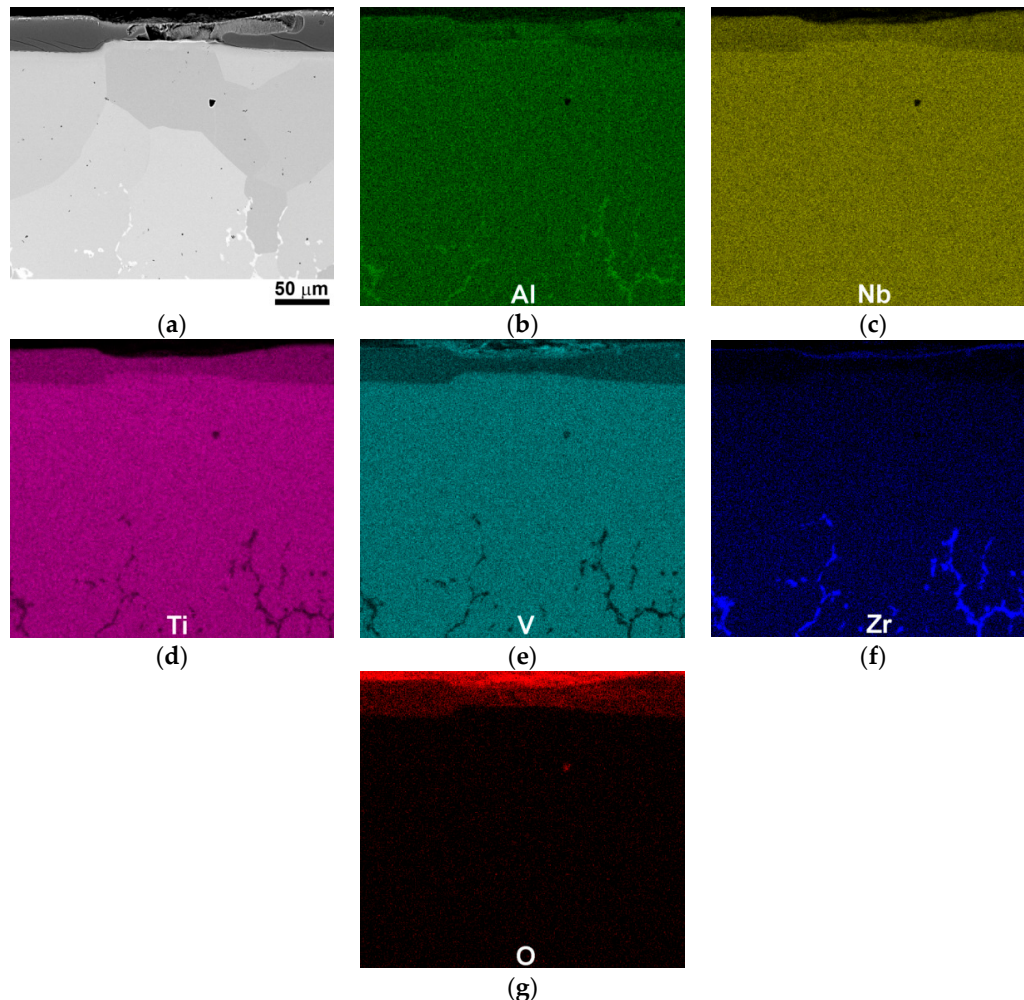
Figure 6. (**a**) SEM-BSE image and (**b**–**g**) corresponded energy-dispersive X-ray spectroscopy (EDS) maps of a cross-section of the $AlNbTiVZr_{0.25}$ alloy after oxidation testing at 600 °C for 100 h.

At 800 °C, the oxide scale was significantly thicker (~800 μm) and had a complex structure (Figure 7a). The top part of the oxide scale (#1 in Figure 7a,b) consisted of a (Al, Nb, V, Ti)-rich OL in a form of whiskers and a layer of mainly needle-shaped (Zr, Nb)-rich oxide particles. According to XRD data (Figures 3 and 4b), the (Al, Nb, V, Ti)-rich OL could be identified as a mixture of the $AlNbO_4$, $TiNb_2O_7$, and VO_2 oxides, whereas the (Zr, Nb)-rich oxide particles—as the $Nb_2Zr_6O_{17}$ oxides. A wide zone with the Ti- and V-rich OLs ("A" in Figure 7a; partly Figure 7b) was observed underneath of the top part; between and inside these OLs, multiple relatively small and separate large pores were found (Figure 7b). The next zone contained numerous relatively small and homogeneously distributed $Nb_2Zr_6O_{17}$ oxide particles ("B" in Figure 7a). A thick layer with the regularly spread $Nb_2Zr_6O_{17}$ oxide particles was situated directly below and expanding till the substrate ("C" in Figure 7a). The distribution of the particles in this layer was very similar to that of the Zr_5Al_3 particles in the substrate (see Figures 1b and 7a).
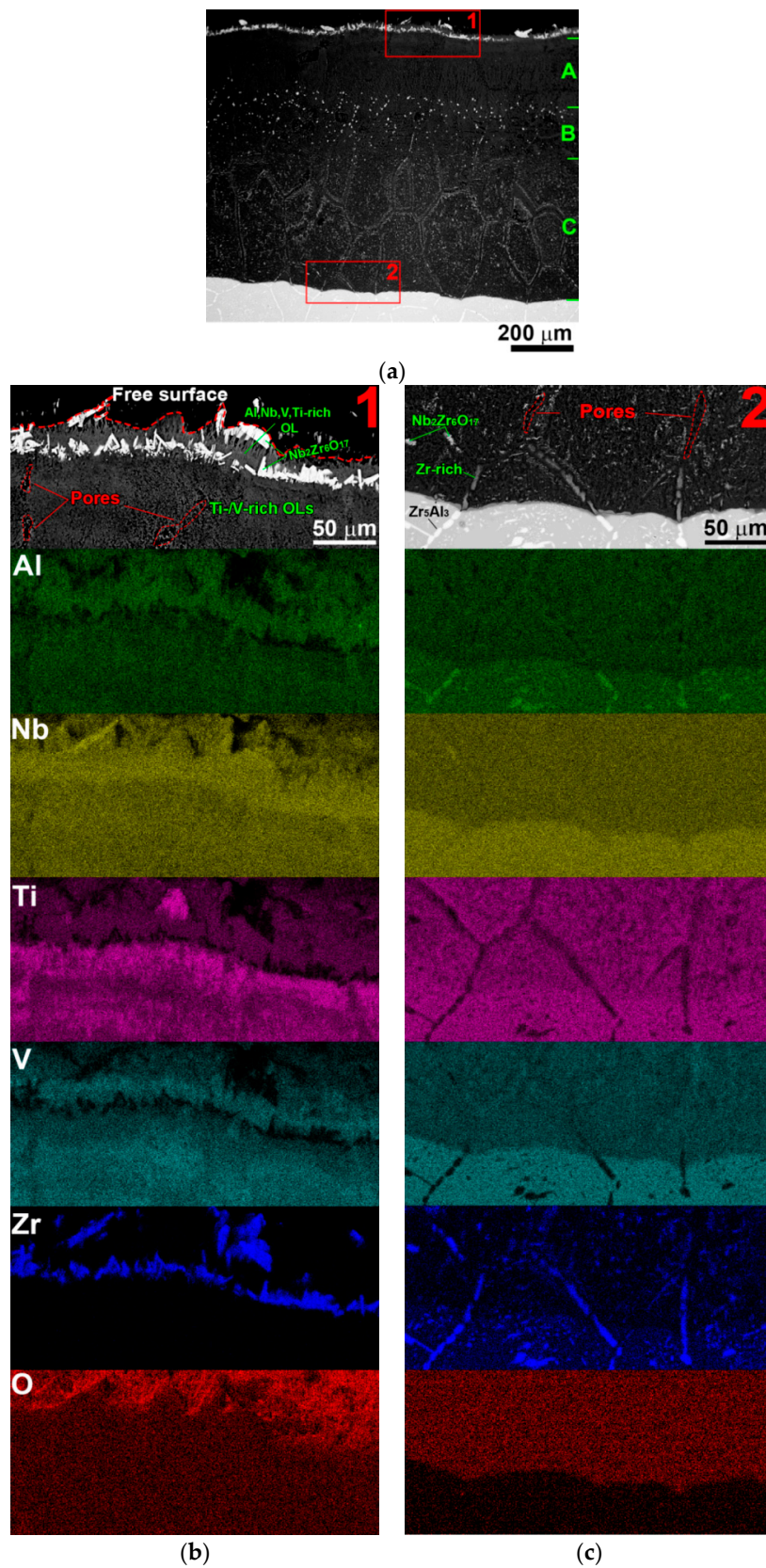
Figure 7. (**a**) SEM-BSE image and (**b**,**c**) combined SEM-BSE-EDS images of (**b**) top part of oxide scale and (**c**) transition zone of a cross-section of the AlNbTiVZr$_{0.25}$ alloy after oxidation testing at 800 °C for 100 h.

A close examination of the transition zone (#2 in Figure 7a,c) revealed some notable features. The oxidation front ascended easily along the Zr_5Al_3 particles but was slightly impeded by the B2 phase. At the boundary between the oxide scale and the un-oxidized substrate, the former Zr_5Al_3 particles started to be depleted with Al which, together with V, segregated to the regions located in the vicinity of these particles. Further, as the oxidation front progressed, Zr-rich particles tended to dissolve with the subsequent formation of the $Nb_2Zr_6O_{17}$ oxide particles on the borders of their previous location. In addition, a lot of pores were found at the former sites of the Zr-rich particles (Figure 7c).

4. Discussion

4.1. Oxidation Kinetics and Mechanisms

The presented results showed that the oxidation behavior of the $AlNbTiVZr_{0.25}$ refractory high-entropy alloy strongly depends on temperature and time. Particularly, at 600–700 °C, the alloy demonstrated a mixed parabolic-linear rate of the mass gain per unit surface area. The same dependences on the double logarithmic scale revealed two distinct stages of oxidation. During the first stage (0–20 h at 600 °C and 0–5 h at 700 °C), oxidation was slow with n = 0.46–0.48. In turn, the second stage (20–100 h at 600 °C and 5–100 h at 700 °C) was characterized by a significantly faster oxidation rate (n = 0.75–0.72).

Most probably, the acceleration of oxidation at the second stage was caused by an effect similar to breakaway oxidation. The breakaway oxidation occurs if many cracks form continuously and propagate quickly through the oxide scale [45]. The oxide scale cracking/spallation was experimentally observed at 600 °C (Figure 6a) and can probably be associated with the changes in the phase composition of the oxide scale. According to XRD data (Figure 4a), the TiO_2 and VO_2, oxides were formed at the beginning of oxidation at 600 °C. Meanwhile, during further (5–10 h) oxidation, the V_2O_5, Nb_2O_5, and $TiNb_2O_7$ oxides started to appear.

The formation of V-rich oxides and subsequent evaporation is reported to be a common reason for significant deterioration of scale adherence in TiAl-based alloys [46–50]; however, this effect is generally observed at T ≥ 700 °C. It should be noted that the decrease in the quantity and intensity of the V_2O_5 oxide diffraction peaks after testing of the $AlNbTiVZr_{0.25}$ alloy at 700 °C can be an indication of its partial evaporation that likely activates the breakaway oxidation at this temperature.

In turn, T = 600 °C is obviously insufficient for the elimination of the VO_2 and V_2O_5 oxides from the surface. Moreover, our analysis revealed the predominance of the V-rich oxides in the form of whiskers at the gas-oxide interface, whereas cracks were found at the oxide-metal interface (Figure 6). This suggests that the VO_2 and V_2O_5 oxides had an only indirect influence on cracking/spallation at 600 °C, rather than being the main reason. In particular, it can be speculated that the whisker-like morphology of the V-rich oxides accelerates the ingress of oxygen through the oxide scale, and thereby leads to the Nb_2O_5 and $TiNb_2O_7$ oxides nucleation in its inner part. The Nb_2O_5 oxide can initially form a protective layer but, with the growth of a scale, induces stresses along the oxide-metal interface, resulting in the scale cracking and breakaway oxidation [36,51]. The complex $TiNb_2O_7$ oxide, which most likely appeared due to the reaction of Nb with TiO_2 and oxygen or as a consequence of the solid-state reaction between Nb_2O_5 and TiO_2 oxides [28,52,53], causes a similar effect [52]. Thus, it can be concluded that the formation of the Nb_2O_5 and $TiNb_2O_7$ oxides at 600 °C allows the metal to oxidize according to an undesirable oxygen-alloy interface reaction process [45] due to the continuous cracking/spallation of the oxide scale.

At 800 °C, the oxidation kinetics obeyed the linear law. This can be due to the formation, from the very beginning of oxidation, of thick, porous oxide scale accompanied by enhanced ingress of gaseous species down to the metal phase [45]. According to XRD analysis, the surface layer consisted, besides the small fraction of the simple ZrO_2 and VO_2 oxides, predominantly of the complex oxides such as $TiNb_2O_7$, $AlNbO_4$, and $Nb_2Zr_6O_{17}$. The similar complex oxides were found after oxidation of the NbTiZrV and AlNbTiZr high-entropy alloys [28,30]. It was reported that the formation of the

$TiNb_2O_7$ and $Nb_2Zr_6O_{17}$ oxides had not improved oxidation resistance, whereas the $AlNbO_4$ oxide formation resulted in sluggish oxidation kinetics. On the contrary, a number of studies demonstrated the detrimental effect of the $AlNbO_4$ oxide on the oxidation resistance [53–57].

Apparently, the studied $AlNbTiVZr_{0.25}$ alloy can be considered as Al-free or V-containing analog of the NbTiZrV or AlNbTiZr alloy, respectively. Our results showed that a hypothetical addition of Al to the NbTiZrV does not lead to an enhancement of the oxidation resistance, but only increases the number of the unprotective complex $TiNb_2O_7$ and $Nb_2Zr_6O_{17}$ oxides due to the $AlNbO_4$ oxide formation. At the same time, a hypothetical doping with V of the AlNbTiZr alloy accelerates oxidation due to the changing of the morphology of the initially protective $AlNbO_4$ oxide, and the formation of the complex $TiNb_2O_7$ and $Nb_2Zr_6O_{17}$ oxides. Thus, it can be hypothesized that a possible positive effect of Al on the oxidation resistance will be neglected in the presence of V even if Al is added in high amounts. V hinders the formation of protective oxides and facilitates the nucleation of unprotective ones. These reactions, in case of the $AlNbTiVZr_{0.25}$ alloy, are most likely driven by the evaporation of volatile V-rich oxides, particularly, the V_2O_5 (Figures 3 and 4b). In addition, the evaporation causes the appearance of multiple pores that serve as places for accelerated ingress of oxygen toward the bare metal and thus stands as the main reason for severe oxidation at 800 °C. It can be assumed that the same processes, but in a more rapid manner, are responsible for the disintegration of the sample tested at 900 °C.

4.2. Comparison with the Conventional Alloys and other RHEAs

Table 4 collects data on the specific mass gains (mg/cm^2) for different alloys, including the examined $AlNbTiVZr_{0.25}$ alloy oxidized at 600–800 °C for 100 h in the air [30,31,50,58–66]. The mass gains of the $AlNbTiVZr_{0.25}$ alloy are comparable with some of the V-based alloys, namely V-30Al [59], Ti-based and TiAl-based alloys with a high V content like Ti-35.5V-14.6Cr-0.32Si-0.11C [62], Ti-15V-3Cr-3Sn-3Al [63], and Ti-42Al-8V-(2-4)Mo [50], and the TiZrNbHfTa RHEA [31]. Note that the $Hf_{0.5}Nb_{0.5}Ta_{0.5}Ti_{1.5}Zr$ alloy suffered from even more severe oxidation due to pesting [29]. However, the mass gains of many other similar alloys at a given temperature interval are significantly lower. Particularly, the mass gain of the V-free AlNbTiZr RHEA at 600–800 °C is ~5–12 times lower than that of the $AlNbTiVZr_{0.25}$ alloy. This finding confirms that V is largely responsible for the poor oxidation resistance of the $AlNbTiVZr_{0.25}$ alloy. In turn, the mass gains of Inconel 690 or orthorhombic (Ti_2AlNb) and gamma (TiAl) alloys after oxidation at 800 °C are lower than the experimentally observed values by 3 or 2 orders of magnitude, respectively (Table 4).

In general, the obtained results demonstrate that despite its promising mechanical properties, the $AlNbTiVZr_{0.25}$ alloy shows rather poor oxidation resistance. This can obviously limit the potential applications of the alloy. To improve the oxidation resistance, modification of the chemical composition, i.e., reduction of the concentration of elements like V or Ti and/or addition or increasing of strong protective scale formers like Al, Cr, or Si is required [23,25–28,31,33]. The alternative approach is to use protective coatings. Particularly, a recent work [32] reported an effective way to improve the oxidation resistance of the $Hf_{0.5}Nb_{0.5}Ta_{0.5}Ti_{1.5}Zr$ RHEA with initially poor oxidation resistance through aluminizing. Nevertheless, the information obtained in the current study can help in the design of RHEAs with a balanced combination of properties including (but not limited to) low density, high strength, sufficient ductility, and good oxidation resistance.

Table 4. Specific mass gains (in mg/cm^2) of different alloys oxidized at 600, 700, and 800 °C for 100 h in the air [30,31,50,58–66].

Temperature	600 °C	700 °C	800 °C	Reference
$AlNbTiVZr_{0.25}$	7.2	38.1	107.5	This study
AlNbTiZr	1.3 [1]	5.6 [1]	8.8 [1]	[30]
TiZrNbHfTa	-	55	-	[31]
$Al_{0.3}TiZrNbHfTa$	-	14	-	[31]
$Al_{0.5}TiZrNbHfTa$	-	14	-	[31]
$Al_{0.75}TiZrNbHfTa$	-	11	-	[31]
AlTiZrNbHfTa	-	10	-	[31]
$Al_{9.2}Cr_{5.7}Hf_{0.5}Mo_{1.3}Nb_{47.0}Ti_{25.9}V_{9.6}W_{0.8}$	-	-	20 [1]	[58]
V-30Al	-	30	84	[59]
V-30Al-10Cr	-	6	31	[59]
V-30Al-10Ti	-	12	29	[59]
V-5Cr-5Ti	~4.5	-	-	[59]
V-9Si-13B	~3	-	-	[61]
Ti-35.5V-14.6Cr-0.32Si-0.11C	-	-	90	[62]
Ti-6Al-4V	-	-	40	[62]
Grade 2	-	-	26.1 [2]	[63]
Ti-15V-3Cr-3Sn-3Al	-	-	174.0 [2]	[63]
Ti-42Al-8V-(2-4)Mo	-	6.7 [3]	92.3 [3]	[50]
Ti-48Al-2Cr-2Nb	-	-	0.9	[64]
Ti-22Al-25Nb	-	-	1.1	[65]
Inconel 690	-	-	0.1	[66]

[1] calculated values; [2] oxidized at 815 °C for 96 h; [3] 100 cycles.

5. Conclusions

In this study, the oxidation behavior of the $AlNbTiVZr_{0.25}$ refractory high-entropy alloy at 600–900 °C was investigated. The following conclusions were made:

(1) At 600–700 °C, two-stage oxidation kinetics was found. Nearly parabolic oxidation (n = 0.46–0.48) at the first stage transitioned to breakaway oxidation (n = 0.75–0.72) at the second stage. The breakaway oxidation was induced by spallation of the oxide scale due to the nucleation of voluminous Nb_2O_5 and $TiNb_2O_7$ oxides at 600 °C, and probably connected with the partial evaporation of the V_2O_5 oxide at 700 °C. At the end of the test (100 h), the surface layers consisted of the V_2O_5, VO_2, TiO_2, Nb_2O_5, $TiNb_2O_7$ oxides at 600 °C, and the V_2O_5, VO_2, TiO_2, Nb_2O_5, $TiNb_2O_7$, ZrO_2, $AlNbO_4$, $Nb_2Zr_6O_{17}$ oxides at 700 °C.

(2) At 800 °C, the oxidation kinetics was nearly linear (n = 0.92). The main reason for severe oxidation were the pores, which served as places for accelerated ingress of oxygen toward the bare metal, and appeared as a result of the evaporation of V-rich oxides, and the formation of a mixture of the complex unprotective $TiNb_2O_7$, $AlNbO_4$, $Nb_2Zr_6O_{17}$ oxides from the very beginning of oxidation. The same oxidation mechanisms were assumed to act at 900 °C that led to the disintegration of the specimen after 50 h.

(3) The oxidation resistance of the alloy can be compared with some V-based/contained alloys. The specific mass gains were estimated to be 7.2, 38.1, and 107.5, and 225.5 mg/cm^2 at 600, 700, and 800 °C for 100 h, and 900 °C for 50 h, respectively.

References

1. Senkov, O.N.; Wilks, G.B.; Miracle, D.B.; Chuang, C.P.; Liaw, P.K. Refractory high-entropy alloys. *Intermetallics* **2010**, *18*, 1758–1765. [CrossRef]

2. Senkov, O.N.; Wilks, G.B.; Scott, J.M.; Miracle, D.B. Mechanical properties of $Nb_{25}Mo_{25}Ta_{25}W_{25}$ and $V_{20}Nb_{20}Mo_{20}Ta_{20}W_{20}$ refractory high entropy alloys. *Intermetallics* **2011**, *19*, 698–706. [CrossRef]

3. Miracle, D.B.; Senkov, O.N. A critical review of high entropy alloys and related concepts. *Acta Mater.* **2017**, *122*, 448–511. [CrossRef]

4. Chen, J.; Zhou, X.; Wang, W.; Liu, B.; Lv, Y.; Yang, W.; Xu, D.; Liu, Y. A review on fundamental of high entropy alloys with promising high-temperature properties. *J. Alloys Compd.* **2018**, *760*, 15–30. [CrossRef]

5. Senkov, O.N.; Miracle, D.B.; Chaput, K.J.; Couzinie, J.-P. Development and exploration of refractory high entropy alloys—A review. *J. Mater. Res.* **2018**, *33*, 3092–3128. [CrossRef]

6. Senkov, O.N.; Woodward, C.F. Microstructure and properties of a refractory $NbCrMo_{0.5}Ta_{0.5}TiZr$ alloy. *Mater. Sci. Eng. A* **2011**, *529*, 311–320. [CrossRef]

7. Senkov, O.N.; Senkova, S.V.; Miracle, D.B.; Woodward, C. Mechanical properties of low-density, refractory multi-principal element alloys of the Cr-Nb-Ti-V-Zr system. *Mater. Sci. Eng. A* **2013**, *565*, 51–62. [CrossRef]

8. Senkov, O.N.; Senkova, S.V.; Woodward, C. Effect of aluminum on the microstructure and properties of two refractory high-entropy alloys. *Acta Mater.* **2014**, *68*, 214–228. [CrossRef]

9. Guo, N.N.; Wang, L.; Luo, L.S.; Li, X.Z.; Su, Y.Q.; Guo, J.J.; Fu, H.Z. Microstructure and mechanical properties of refractory MoNbHfZrTi high-entropy alloy. *Mater. Des.* **2015**, *81*, 87–94. [CrossRef]

10. Juan, C.C.; Tsai, M.H.; Tsai, C.W.; Lin, C.M.; Wang, W.R.; Yang, C.C.; Chen, S.K.; Lin, S.J.; Yeh, J.W. Enhanced mechanical properties of HfMoTaTiZr and HfMoNbTaTiZr refractory high-entropy alloys. *Intermetallics* **2015**, *62*, 76–83. [CrossRef]

11. Yurchenko, N.Y.; Stepanov, N.D.; Shaysultanov, D.G.; Tikhonovsky, M.A.; Salishchev, G.A. Effect of Al content on structure and mechanical properties of the $Al_xCrNbTiVZr$ (x = 0; 0.25; 0.5; 1) high-entropy alloys. *Mater. Charact.* **2016**, *121*, 125–134. [CrossRef]

12. Han, Z.D.; Chen, N.; Zhao, S.F.; Fan, L.W.; Yang, G.N.; Shao, Y.; Yao, K.F. Effect of Ti additions on mechanical properties of NbMoTaW and VNbMoTaW refractory high entropy alloys. *Intermetallics* **2017**, *84*, 153–157. [CrossRef]

13. Chen, H.; Kauffmann, A.; Gorr, B.; Schliephake, D.; Seemüller, C.; Wagner, J.N.; Christ, H.J.; Heilmaier, M. Microstructure and mechanical properties at elevated temperatures of a new Al-containing refractory high-entropy alloy Nb-Mo-Cr-Ti-Al. *J. Alloys Compd.* **2016**, *661*, 206–215. [CrossRef]

14. Senkov, O.N.; Scott, J.M.; Senkova, S.V.; Miracle, D.B.; Woodward, C.F. Microstructure and room temperature properties of a high-entropy TaNbHfZrTi alloy. *J. Alloys Compd.* **2011**, *509*, 6043–6048. [CrossRef]

15. Wu, Y.D.; Cai, Y.H.; Wang, T.; Si, J.J.; Zhu, J.; Wang, Y.D.; Hui, X.D. A refractory $Hf_{25}Nb_{25}Ti_{25}Zr_{25}$ high-entropy alloy with excellent structural stability and tensile properties. *Mater. Lett.* **2014**, *130*, 277–280. [CrossRef]

16. Sheikh, S.; Shafeie, S.; Hu, Q.; Ahlström, J.; Persson, C.; Veselý, J.; Zýka, J.; Klement, U.; Guo, S. Alloy design for intrinsically ductile refractory high-entropy alloys. *J. Appl. Phys.* **2016**, *120*, 164902. [CrossRef]

17. Juan, C.-C.; Tseng, K.-K.; Hsu, W.-L.; Tsai, M.-H.; Tsai, C.-W.; Lin, C.-M.; Chen, S.-K.; Lin, S.-J.; Yeh, J.-W. Solution strengthening of ductile refractory $HfMo_xNbTaTiZr$ high-entropy alloys. *Mater. Lett.* **2016**, *175*, 284–287. [CrossRef]

18. Wu, Y.; Si, J.; Lin, D.; Wang, T.; Wang, W.Y.; Wang, Y.; Liu, Z.; Hui, X. Phase stability and mechanical properties of AlHfNbTiZr high-entropy alloys. *Mater. Sci. Eng. A* **2018**, *724*, 249–259. [CrossRef]

19. Senkov, O.N.; Semiatin, S.L. Microstructure and properties of a refractory high-entropy alloy after cold working. *J. Alloys Compd.* **2015**, *649*, 1110–1123. [CrossRef]

20. Senkov, O.N.; Pilchak, A.L.; Semiatin, S.L. Effect of Cold Deformation and Annealing on the Microstructure and Tensile Properties of a HfNbTaTiZr Refractory High Entropy Alloy. *Metall. Mater. Trans. A* **2018**, *49*, 2876–2892. [CrossRef]

21. Wu, W.; Ni, S.; Liu, Y.; Song, M. Effects of cold rolling and subsequent annealing on the microstructure of a HfNbTaTiZr high-entropy alloy. *J. Mater. Res.* **2016**, *31*, 3815–3823. [CrossRef]

22. Juan, C.-C.; Tsai, M.-H.; Tsai, C.-W.; Hsu, W.-L.; Lin, C.-M.; Chen, S.-K.; Lin, S.-J.; Yeh, J.-W. Simultaneously increasing the strength and ductility of a refractory high-entropy alloy via grain refining. *Mater. Lett.* **2016**, *184*, 200–203. [CrossRef]

23. Senkov, O.N.; Senkova, S.V.; Dimiduk, D.M.; Woodward, C.; Miracle, D.B. Oxidation behavior of a refractory NbCrMo$_{0.5}$Ta$_{0.5}$TiZr alloy. *J. Mater. Sci.* **2012**, *47*, 6522–6534. [CrossRef]

24. Liu, C.M.; Wang, H.M.; Zhang, S.Q.; Tang, H.B.; Zhang, A.L. Microstructure and oxidation behavior of new refractory high entropy alloys. *J. Alloys Compd.* **2014**, *583*, 162–169. [CrossRef]

25. Gorr, B.; Azim, M.; Christ, H.J.; Mueller, T.; Schliephake, D.; Heilmaier, M. Phase equilibria, microstructure, and high temperature oxidation resistance of novel refractory high-entropy alloys. *J. Alloys Compd.* **2015**, *624*, 270–278. [CrossRef]

26. Gorr, B.; Mueller, F.; Christ, H.-J.; Mueller, T.; Chen, H.; Kauffmann, A.; Heilmaier, M. High temperature oxidation behavior of an equimolar refractory metal-based alloy 20Nb20Mo20Cr20Ti20Al with and without Si addition. *J. Alloys Compd.* **2016**, *688*, 468–477. [CrossRef]

27. Gorr, B.; Müller, F.; Azim, M.; Christ, H.-J.; Müller, T.; Chen, H.; Kauffmann, A.; Heilmaier, M. High-Temperature Oxidation Behavior of Refractory High-Entropy Alloys: Effect of Alloy Composition. *Oxid. Met.* **2017**, *88*, 339–349. [CrossRef]

28. Butler, T.M.; Chaput, K.J.; Dietrich, J.R.; Senkov, O.N. High temperature oxidation behaviors of equimolar NbTiZrV and NbTiZrCr refractory complex concentrated alloys (RCCAs). *J. Alloys Compd.* **2017**, *729*, 1004–1019. [CrossRef]

29. Sheikh, S.; Bijaksana, M.K.; Motallebzadeh, A.; Shafeie, S.; Lozinko, A.; Gan, L.; Tsao, T.-K.; Klement, U.; Canadinc, D.; Murakami, H.; et al. Accelerated oxidation in ductile refractory high-entropy alloys. *Intermetallics* **2018**, *97*, 58–66. [CrossRef]

30. Jayaraj, J.; Thirathipviwat, P.; Han, J.; Gebert, A. Microstructure, mechanical and thermal oxidation behavior of AlNbTiZr high entropy alloy. *Intermetallics* **2018**, *100*, 9–19. [CrossRef]

31. Chang, C.; Titus, M.S.; Yeh, J. Oxidation Behavior between 700 and 1300 °C of Refractory TiZrNbHfTa High-Entropy Alloys Containing Aluminum. *Adv. Eng. Mater.* **2018**, *20*, 1700948. [CrossRef]

32. Sheikh, S.; Gan, L.; Tsao, T.; Murakami, H.; Shafeie, S.; Guo, S. Aluminizing for enhanced oxidation resistance of ductile refractory high-entropy alloys. *Intermetallics* **2018**, *103*, 40–51. [CrossRef]

33. Waseem, O.A.; Auyeskhan, U.; Lee, H.M.; Ryu, H.J. A combinatorial approach for the synthesis and analysis of Al$_x$Cr$_y$Mo$_z$NbTiZr high-entropy alloys: Oxidation behavior. *J. Mater. Res.* **2018**, *33*, 3226–3234. [CrossRef]

34. Yurchenko, N.Y.; Stepanov, N.D.; Zherebtsov, S.V.; Tikhonovsky, M.A.; Salishchev, G.A. Structure and mechanical properties of B2 ordered refractory AlNbTiVZr$_x$ (x = 0–1.5) high-entropy alloys. *Mater. Sci. Eng. A* **2017**, *704*, 82–90. [CrossRef]

35. Yurchenko, N.Y.; Stepanov, N.D.; Gridneva, A.O.; Mishunin, M.V.; Salishchev, G.A.; Zherebtsov, S.V. Effect of Cr and Zr on phase stability of refractory Al-Cr-Nb-Ti-V-Zr high-entropy alloys. *J. Alloys Compd.* **2018**, *757*, 403–414. [CrossRef]

36. Birks, N.; Meier, G.; Pettit, F. *Introduction to the High Temperature Oxidation of Metals*, 2nd ed.; Cambridge University Press: Cambridge, UK, 2006; ISBN 9781139163903.

37. Bose, M.; Basu, A. ^{51}V NMR of the layered δ-LiV$_2$O$_5$. *J. Solid State Chem.* **1989**, *81*, 30–34. [CrossRef]

38. Oka, Y.; Sato, S.; Yao, T.; Yamamoto, N. Crystal Structures and Transition Mechanism of VO$_2$(A). *J. Solid State Chem.* **1998**, *141*, 594–598. [CrossRef]

39. Kim, D.-W.; Enomoto, N.; Nakagawa, Z.; Kawamura, K. Molecular Dynamic Simulation in Titanium Dioxide Polymorphs: Rutile, Brookite, and Anatase. *J. Am. Ceram. Soc.* **1996**, *79*, 1095–1099. [CrossRef]

40. Ercit, T.S. Refinement of the Structure of ζ-Nb$_2$O$_5$ and Its Relationship to the Rutile and Thoreaulite Structures. *Mineral. Petrol.* **1991**, *43*, 217–223. [CrossRef]

41. Gasperin, M. Affinement de la structure de TiNb$_2$O$_7$ et répartition des cations. *J. Solid State Chem.* **1984**, *53*, 144–147. [CrossRef]

42. Howard, C.J.; Hill, R.J. The polymorphs of zirconia: Phase abundance and crystal structure by Rietveld analysis of neutron and X-ray diffraction data. *J. Mater. Sci.* **1991**, *26*, 127–134. [CrossRef]

43. Greis, O.; Ziel, R.; García, D.E.; Claussen, N.; Breidenstein, B.; Haase, A. Crystal Structure and Morphology of Disordered AlNbO$_4$ from X-Ray Powder Diffraction. *Mater. Sci. Forum* **1996**, *228–231*, 825–830. [CrossRef]

44. Galy, J.; Roth, R.S. The crystal structure of Nb$_2$Zr$_6$O$_{17}$. *J. Solid State Chem.* **1973**, *7*, 277–285. [CrossRef]

45. Korb, L.J.; Olson, D.L. Volume 13A: Corrosion: Fundamentals, Testing, and Protection. In *ASM Handbook*; ASM International Committee: Geauga, OH, USA, 1987; pp. 1–3455.

46. Kim, B.G.; Kim, G.M.; Kim, C.J. Oxidation Behavior of TiAl-X (X = Cr, V, Si, Mo or Nb) Intermetallics at Elevated Temperature. *Scr. Metall. Mater.* **1995**, *33*, 1117–1125. [CrossRef]

47. Shida, Y.; Anada, H. The Effect of Various Ternary Additives on the Oxidation Behavior of TiAl in High-Temperature Air. *Oxid. Met.* **1996**, *45*, 197–219. [CrossRef]

48. Lee, D.B.; Jang, Y.D. High Temperature Oxidation of Ti39.4Al10V Alloy. *Mater. Sci. Forum* **2004**, *452*, 813–816. [CrossRef]

49. Lee, D. Effect of Cr, Nb, Mn, V, W and Si on High Temperature Oxidation of TiAl Alloys. *Met. Mater. Int.* **2005**, *11*, 141–147. [CrossRef]

50. Naveed, M.; Renteria, A.F.; Weiß, S. Role of alloying elements during thermocyclic oxidation of β/γ-TiAl alloys at high temperatures. *J. Alloys Compd.* **2017**, *691*, 489–497. [CrossRef]

51. Rapp, R.A. Kinetics, Microstructures and Mechanism of Internal Oxidation-Its Effect and Prevention in High Temperature Alloy Oxidation. *Corrosion* **1965**, *21*, 382–401. [CrossRef]

52. Parida, S.C.; Gupta, N.K.; Krishnan, K.; Rao, G.A.R.; Sen, B.K. High-Temperature Oxidation of β-NbTi Alloys. *Metall. Mater. Trans. A* **2008**, *39*, 2020–2025. [CrossRef]

53. Jiang, H. Effect of Nb on the high temperature oxidation of Ti-(0–50 at.%)Al. *Scr. Mater.* **2002**, *46*, 639–643. [CrossRef]

54. Ralison, A.; Dettenwanger, F.; Schütze, M. Oxidation of orthorhombic Ti_2AlNb alloys at 800 °C in air. *Mater. Corros.* **2000**, *328*, 317–328. [CrossRef]

55. Leyens, C. Environmental Effects on Orthorhombic Alloy Ti-22Al-25Nb in Air between 650 and 1000 °C. *Oxid. Met.* **2000**, *54*, 475–503.

56. Leyens, C. Oxidation of Orthorhombic Titanium Aluminide Ti-22Al-25Nb in Air between 650 and 1000 °C. *J. Mater. Eng. Perform.* **2001**, *10*, 225–230. [CrossRef]

57. He, Y. Oxidation behavior of a novel multi-element alloyed Ti_2AlNb- based alloy in temperature range of 650–850 °C. *Rare Met.* **2018**, *37*, 838–845. [CrossRef]

58. Zheng, J.; Hou, X.; Wang, X.; Meng, Y.; Zheng, X.; Zheng, L. Isothermal oxidation mechanism of a newly developed Nb-Ti-V-Cr-Al-W-Mo-Hf alloy at 800–1200 °C. *Int J. Refract. Met. Hard Mater.* **2016**, *54*, 322–329. [CrossRef]

59. Keller, J.G. The High-Temperature Oxidation Behavior of Vanadium-Aluminum Alloys. *Oxid. Met.* **1991**, *36*, 439–464. [CrossRef]

60. Natesan, K.; Uz, M. Oxidation performance of V-Cr-Ti alloys. *Fusion Eng. Des.* **2000**, *52*, 145–152. [CrossRef]

61. Krüger, M. High temperature compression strength and oxidation of a V-9Si-13B alloy. *Scr. Mater.* **2016**, *121*, 75–78. [CrossRef]

62. Mi, G.; Yao, K.; Bai, P.; Cheng, C.; Min, X. High Temperature Oxidation and Wear Behaviors of Ti–V–Cr Fireproof Titanium Alloy. *Metals* **2017**, *7*, 226. [CrossRef]

63. Bania, P.J. Next Generation Titanium Alloys for Elevated Temperature Service. *ISIJ Int.* **1991**, *31*, 840–847. [CrossRef]

64. Haanappel, V.A.C.; Clemens, H.; Stroosnijder, M.F. The high temperature oxidation behaviour of high and low alloyed TiAl-based intermetallics. *Intermetallics* **2002**, *10*, 293–305. [CrossRef]

65. Leyens, C.; Gedanitz, H. Long-Term Oxidation of Orthorhombic Alloy Ti-22Al-25Nb in Air between 650 and 800 °C. *Scr. Mater.* **1999**, *41*, 901–906. [CrossRef]

66. Hussain, N.; Shahid, K.A.; Khan, I.H.; Rahman, S. Oxidation of High-Temperature Alloys (Superalloys) at Elevated Temperatures in Air. II. *Oxid. Met.* **1995**, *43*, 363–378. [CrossRef]